NASA/TM-20205008430



Analysis of 2018 Aerothermal Calibration Test at NASA Propulsion Systems Laboratory

Paul H. von Hardenberg and Peter M. Struk
Glenn Research Center, Cleveland, Ohio

Tadas P. Bartkus
Ohio Aerospace Institute, Brook Park, Ohio

Michael J. Oliver
Glenn Research Center, Cleveland, Ohio

Aaron Johnson
Jacobs Technology, Brook Park, Ohio

December 2020

NASA STI Program . . . in Profile

Since its founding, NASA has been dedicated to the advancement of aeronautics and space science. The NASA Scientific and Technical Information (STI) Program plays a key part in helping NASA maintain this important role.

The NASA STI Program operates under the auspices of the Agency Chief Information Officer. It collects, organizes, provides for archiving, and disseminates NASA's STI. The NASA STI Program provides access to the NASA Technical Report Server—Registered (NTRS Reg) and NASA Technical Report Server—Public (NTRS) thus providing one of the largest collections of aeronautical and space science STI in the world. Results are published in both non-NASA channels and by NASA in the NASA STI Report Series, which includes the following report types:

- TECHNICAL PUBLICATION. Reports of completed research or a major significant phase of research that present the results of NASA programs and include extensive data or theoretical analysis. Includes compilations of significant scientific and technical data and information deemed to be of continuing reference value. NASA counter-part of peer-reviewed formal professional papers, but has less stringent limitations on manuscript length and extent of graphic presentations.

- TECHNICAL MEMORANDUM. Scientific and technical findings that are preliminary or of specialized interest, e.g., "quick-release" reports, working papers, and bibliographies that contain minimal annotation. Does not contain extensive analysis.

- CONTRACTOR REPORT. Scientific and technical findings by NASA-sponsored contractors and grantees.

- CONFERENCE PUBLICATION. Collected papers from scientific and technical conferences, symposia, seminars, or other meetings sponsored or co-sponsored by NASA.

- SPECIAL PUBLICATION. Scientific, technical, or historical information from NASA programs, projects, and missions, often concerned with subjects having substantial public interest.

- TECHNICAL TRANSLATION. English-language translations of foreign scientific and technical material pertinent to NASA's mission.

For more information about the NASA STI program, see the following:

- Access the NASA STI program home page at http://www.sti.nasa.gov

- E-mail your question to help@sti.nasa.gov

- Fax your question to the NASA STI Information Desk at 757-864-6500

- Telephone the NASA STI Information Desk at 757-864-9658

- Write to:
  NASA STI Program
  Mail Stop 148
  NASA Langley Research Center
  Hampton, VA 23681-2199

NASA/TM-20205008430



Analysis of 2018 Aerothermal Calibration Test at NASA Propulsion Systems Laboratory

Paul H. von Hardenberg and Peter M. Struk
Glenn Research Center, Cleveland, Ohio

Tadas P. Bartkus
Ohio Aerospace Institute, Brook Park, Ohio

Michael J. Oliver
Glenn Research Center, Cleveland, Ohio

Aaron Johnson
Jacobs Technology, Brook Park, Ohio

National Aeronautics and
Space Administration

Glenn Research Center
Cleveland, Ohio 44135

December 2020

This work was sponsored by the Advanced Air Vehicle Program
at the NASA Glenn Research Center

Trade names and trademarks are used in this report for identification only. Their usage does not constitute an official endorsement, either expressed or implied, by the National Aeronautics and Space Administration.

Level of Review: This material has been technically reviewed by technical management.

Available from

NASA STI Program
Mail Stop 148
NASA Langley Research Center
Hampton, VA 23681-2199

National Technical Information Service
5285 Port Royal Road
Springfield, VA 22161
703-605-6000

This report is available in electronic form at http://www.sti.nasa.gov/ and http://ntrs.nasa.gov/

Analysis of 2018 Aerothermal Calibration Test at NASA Propulsion Systems Laboratory

Paul H. von Hardenberg and Peter M. Struk
National Aeronautics and Space Administration
Glenn Research Center
Cleveland, Ohio 44135

Tadas P. Bartkus
Ohio Aerospace Institute
Brook Park, Ohio 44142

Michael J. Oliver
National Aeronautics and Space Administration
Glenn Research Center
Cleveland, Ohio 44135

Aaron Johnson
Jacobs Technology
Brook Park, Ohio 44142

Summary

This report documents some of the key findings from an aerothermal calibration test that was conducted at the NASA Propulsion Systems Laboratory (PSL) as part of a series of fundamental ice-crystal icing tests in 2018. The purpose of the aerothermal calibration test was to characterize the cloud-off temperature and flow of the PSL test facility prior to performing the cloud-on icing experiments. This report presents the temperature measurements and analysis of that test day, which examined uniformity and the influence of spray bars and wall temperature effects. Air temperature profiles were measured just upstream of the test section, and at the test section, for several cases across a range of parameters, including, but not limited to, spray-bar air temperature (T_{nozz}), altitude, airflow velocity, and spray-bar atomizing pressure (P_{nozz}). The data suggests that P_{nozz} may have a small effect on the downstream temperature when T_{nozz} is equal to the plenum temperature of 7.2 °C (45 °F) at a flow speed of 85 m/s, but it was difficult to establish a trend for that set of data. However, there was no effect of increasing P_{nozz} at the higher flow velocities that were tested. When T_{nozz} was heated to 82.2 °C (180 °F), the effect of increasing the P_{nozz} has a more significant effect on the temperature at the test section, which could increase by as much as 3 °C (5.4 °F) as a result. In addition, the data show that the ambient air surrounding the PSL exit duct, which is typically near room temperature, can cause the airflow to have warmer temperatures near the duct wall than at the centerline resulting in parabolic temperature profiles. However, the effects from the ambient air surrounding the duct are reduced at higher flow velocities resulting in flatter and more uniform temperature profiles. Finally, this report presents some comparisons between the various temperature measurement probes used during testing as well as the effect of self-heating for probes that used heat for anti-icing.

Nomenclature

P	pressure, kPa (absolute)
P_{nozz}	spray-bar atomizing air pressure supplied to nozzles, kPa (gauge)
PSL	NASA Propulsion Systems Laboratory
RFP	rearward facing probe
R_{RFP}	radial position of the RFP
RH	relative humidity, percent
TAT	total air temperature, °C
TC	thermocouple
TPL	total temperature at the plenum, °C
TR	test run
T	temperature, °C
T_{corr}	total temperature measured at test section (after correction factors), °C
T_m	total temperature measured at test section (before correction factors), °C
T_{nozz}	spray-bar atomizing air temperature supplied to nozzles, °C
T_r	recovery temperature, °C
T_{RFP}	total temperature measured by RFP, °C
T_{TAT}	total temperature measured by Rosemount TAT probe, °C
$T_{TC\#}$	total temperature measured by thermocouple, °C
V_e	air exit velocity through calibration duct, m/s
ΔT	temperature, delta, $T_{corr} - T_{0,i}$, °C
η	recovery correction variable

Subscripts

0	total or plenum conditions
i	inlet condition (at spray bars)
e	exit or test section condition
corr	correction factors applied to measurement
m	raw measurement (before correction factors)
heat-off	deicing heat element turned off
heat-on	deicing heat element turned on

1.0 Introduction

Ice-crystal ingestion at high altitudes has been attributed to some jet engine power-loss events due to icing that occurs in the core compressor regions of a jet engine (Ref. 1). NASA's Propulsion Systems Laboratory (PSL) is a high-altitude jet-engine test facility that has recently added the capability to inject ice particles upstream of an operating jet engine (Ref. 2). The ice particles are created upstream of the test area using liquid-water spray nozzles that produce water droplets. The water droplets freeze prior to reaching the test section due to a combination of evaporative and convective cooling. Many successful tests using jet engines have been conducted at PSL to investigate ice-crystal icing inside a jet engine (Refs. 3 to 5).

Due to spatial restrictions, it is difficult to implement the instrumentation necessary to study ice accretions in well-characterized conditions from within a jet engine. As an alternative, NASA is simulating the internal conditions of a jet engine using an external flow environment using the PSL facility. The fundamental icing physics tests at the PSL facility expand upon similar investigations that were done in collaboration with the National Research Council Canada that began in 2010 (Refs. 6 to 8). The primary objective of the fundamental icing physics tests is to gain a better understanding of the physics behind ice formation within jet engines and to validate and improve ice-accretion models for current and future aircraft (Refs. 9 to 17). The conditions to be controlled include the air wet-bulb temperature, particle size distribution, and melted portion of incoming ice particle cloud. At the test section, the icing parameters being measured include the total water content, melt ratio, particle size distribution, and aerothermal conditions such as pressure, velocity, temperature, and humidity.

In June 2018, an experiment on ice-crystal icing was conducted at PSL with the goal of creating a set of ice shapes on a NACA 0012 airfoil under well-characterized conditions to help develop and validate ice-crystal icing models (Ref. 18). The June 2018 test built upon the results of a similar test at the PSL in 2016 (Ref. 19). The purpose of this report is to document some of the key findings from the aerothermal calibration data that was recorded on June 4, 2018. The specific test objectives, approach, results, and conclusion of the aerothermal calibration test are discussed in the subsequent sections.

2.0 Objectives

Air temperature is one of the most fundamental measurements in icing research—temperature changes of just a degree or two in Celsius can dramatically change an icing event or even transition from an icing to nonicing condition. One test day was dedicated for a standard aerothermal calibration test that included detailed measurements of the air temperature profiles at the test section in PSL. There is evidence from previous testing that the spray-bar air and water temperatures affect the total air temperature (TAT) at the test section prior to spray initiation. It is important to separate that effect from others (such as cloud evaporation cooling effect) on the air temperature at the test section.

Specific objectives for the aerothermal calibration test include measurements of the radial air temperature profiles across the test section for different conditions by varying the following facility control parameters:

- V_e (air exit velocity through calibration duct)
- Altitude
- Spray-bar atomizing air and water temperatures
- Atomizing air pressure

The radial air temperature measurements were primarily captured using a thermocouple (TC) rake assembly (referred to as the “sword rake”). The 2018 experiment at PSL also featured a new instrument traversing system that allowed surveys of the flow, downstream of the sword rake, with intrusive probes that included a commercial Rosemount Aerospace Inc., TAT probe (model 102LJ2AG) (Collins Aerospace) and a custom rearward facing probe (RFP) that measured both temperature and humidity. The RFP was used to measure TAT and humidity in the presence of the cloud although the data presented in this report focuses on the cloud-off probe thermal response. More details on the various instrumentation can be found in the literature (Refs. 20 to 22) and following sections. In this report, cross-comparisons of the sword rake data to the TAT probe, which were not in the same axial plane, are presented.

3.0 Approach

The aerothermal calibration test was conducted at the NASA Glenn PSL. A side profile of the PSL facility depicting the duct dimensions and relative locations of the spray bars, sword rake, and traversing mechanism is shown in Figure 1. Please note that information regarding the axial location of the sword rake was unable to be retrieved at the time of writing this report, so the location has been denoted by distance "X."

The aerothermal calibration test matrix used three different target velocities (85, 135, and 185 m/s) and two different total pressures (44.8 and 87.6 kPa) that covered the range of testing for the 2018 PSL icing tests. In addition, two different spray-bar air temperatures of 7.2 °C (45 °F) and 82.2 °C (180 °F) were used (water and air were circulating through the spray bars but not spraying). A single total plenum air temperature, $T_{0,i}$ (or TPL), of 7.2 °C was used for all the testing. Table 1 shows the target conditions for each of the seven cases that were tested.

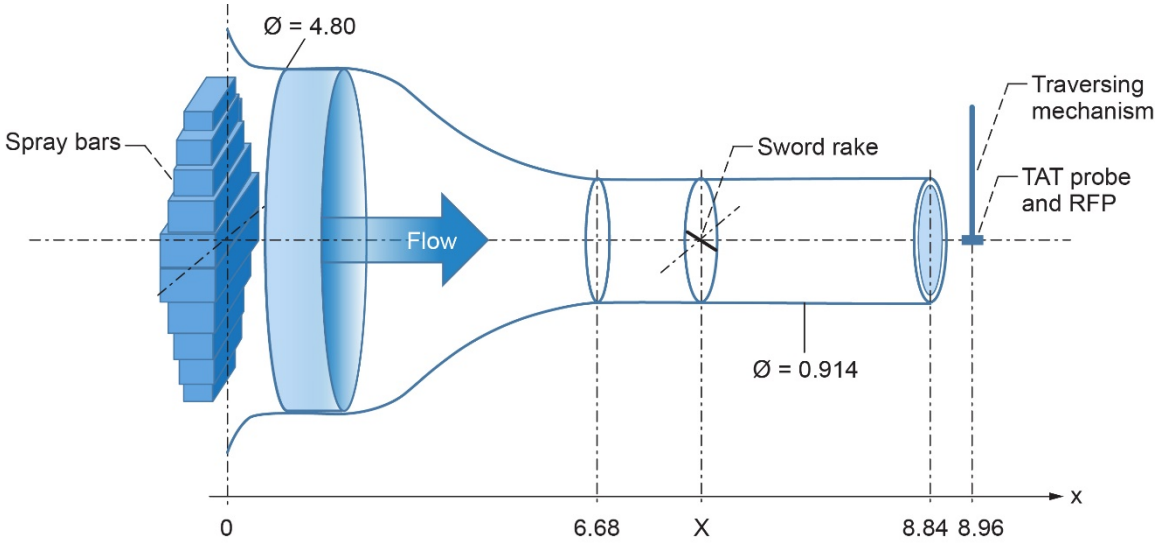

Figure 1.—Propulsion Systems Laboratory (PSL) side profile. Total air temperature (TAT). Rearward facing probe (RFP). Dimensions are in meters. Not to scale.

TABLE 1.—TARGET CONDITIONS FOR JUNE 2018 AEROTHERMAL CALIBRATION TEST

Case	$T_{0,i}$,[a] °C	$RH_{0,i}$,[b] percent	$P_{0,i}$,[c] kPa	V_e,[d] m/s	T_{nozz},[e] °C	Test run, TR
1	7.2	0	87.6	85	7.2	3 to 17
2	7.2	0	87.6	135	7.2	18 to 24
3	7.2	0	87.6	185	7.2	25 to 34
4	7.2	0	44.8	85	7.2	35 to 39
5	7.2	0	44.8	185	7.2	40 to 42
6	7.2	0	44.8	185	82.2	43 to 45
7	7.2	0	44.8	85	82.2	46

[a]Total plenum air temperature.
[b]Relative humidity.
[c]Total plenum pressure.
[d]Air exit velocity through calibration duct.
[e]Spray-bar atomizing air temperature.

Each test point started with the atomizing air pressure off. Once stabilized and data recorded, spray-bar atomizing air pressures supplied to the nozzles (P_{nozz}) was increased to see the effect on the measured temperature at the test section—increasing the atomizing air pressure introduces a small air mass flow into the facility. The P_{nozz} during the test were 0, 34.5, 68.9, 138, 345, and 621 kPa (gauge).

Figure 2 shows the polar coordinates of the TCs, RFP, and the traversed locations of the TAT probe along the sword rake as seen from an observer standing aft and looking upstream of the flow. Also seen in Figure 2 are the TC locations that measured the inner and outer metal temperatures along the circumference of the duct wall. It should be noted that the axial locations of the sword rake, duct wall TCs, RFP, and TAT probe were not the same (see Figure 1). The sword rake did not have a TC at the centerline. Centerline temperature measurements were made using the TAT probe. Subsequently, the TAT probe and RFP were traversed (separately) along the sword rake positions to compare their temperature measurements to the TC measurements at the corresponding locations along the sword rake. Finally, the PSL facility measures $T_{0,i}$ using the average of 17 type-K TCs. The TCs are mounted along the horizontal and vertical diameters of the PSL plenum just upstream of the spray bars.

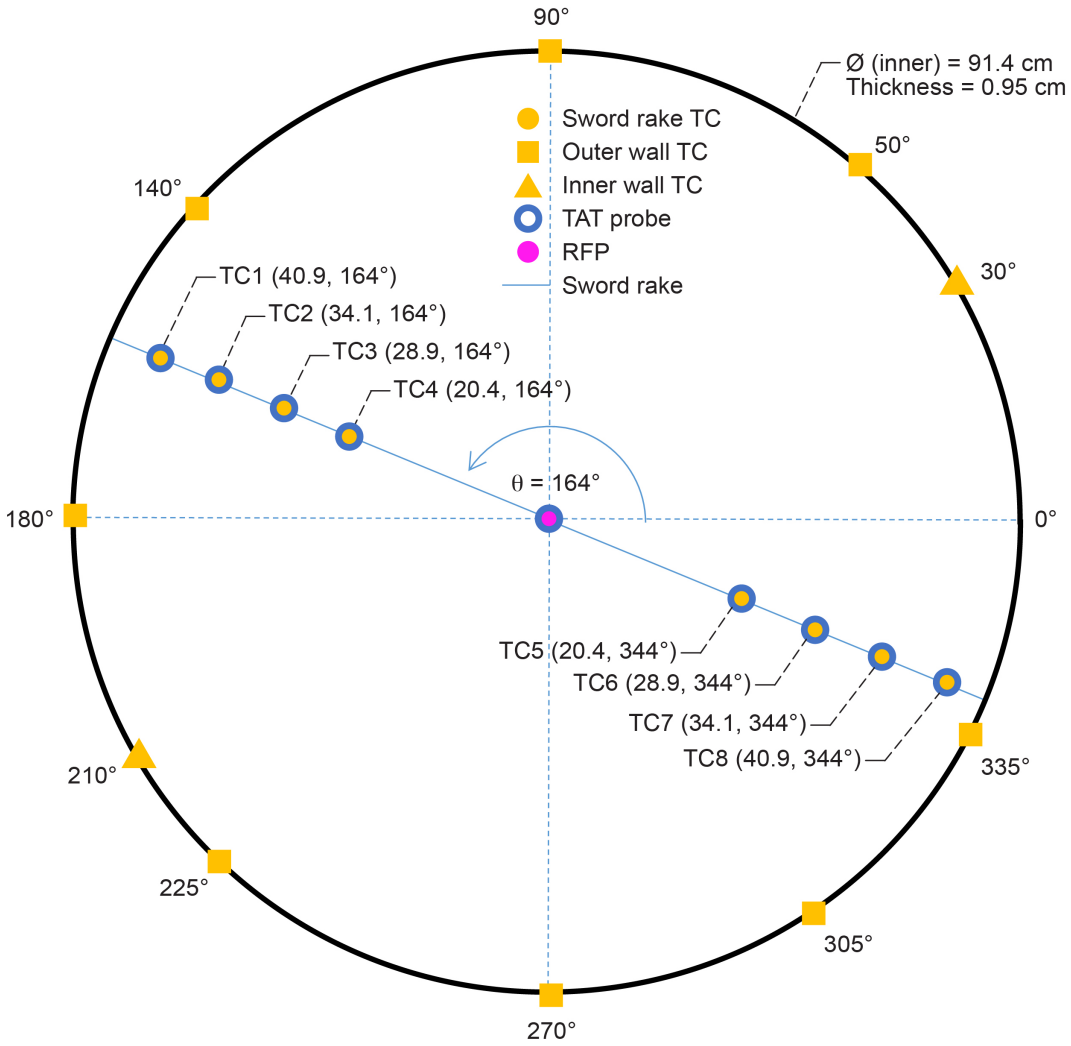

Figure 2.—Sword rake probe locations (aft looking forward). Total air temperature (TAT). Thermocouple (TC). Rearward facing probe (RFP). Dimensions and coordinate system are in centimeters.

4.0 Results and Analysis

This section presents the various temperature measurements obtained during the test. Radial temperature profiles of the test section are analyzed for different spray-bar atomizing pressures and temperatures. Temperature measurements taken during the TAT probe traverse tests are compared to the TC temperature measurements along the sword rake. Recovery corrections applied to the TAT probe, TCs, and RFP temperature measurements are described. Lastly, the influence of deicing heat applied to the TAT probe on the temperature measurements are investigated.

4.1 Temperature Measurement Corrections

Recovery corrections were applied to the Rosemount TAT probe and sword rake TC measurements to compensate for the incomplete conversion of kinetic energy of the flowing air. This is especially important at high Mach numbers when the recovery of the kinetic energy is the least due to increased thermal and viscous losses when the flow encounters the probe body. The recovery correction factors used for the TC data at various Mach numbers are shown in Table 2. The correction factors are the ratio of the measured to actual total temperature. These values were obtained from an independent calibration of the sword rake in a free-jet test facility at NASA Glenn (see Appendix). The corrections were approximately the same for each of the eight TC positions and thus the same correction was applied for each TC on the sword rake for a given Mach number. The recovery correction factors for the TAT probe can be found in the guide provided by the manufacturer (Ref. 20). A second-order polynomial curve fit was applied to interpolate the correction factors at the Mach numbers used during the test. However, the wall TC measurements were not corrected as the flow velocity is essentially zero at the wall interface.

Care was taken to ensure that the average temperature values were obtained from the steady-state durations of the test only. This was particularly important for the test runs in which data recordings began during PSL startup or when the facility was transitioning from one test condition to the next. Typically, the data recordings for these test runs were long (10+ min) and only the last 2 min were considered to be at a steady-state condition and used for analysis purposes. Once the steady-state portions of the test were determined, the average temperature during that timespan was calculated.

4.2 Radial Air Temperature Measurements

Figure 3 to Figure 6 show ΔT as a function of radial distance for various nozzle air pressure conditions, where ΔT is defined as the difference between the temperature measured (and corrected) at the test section and the temperature at the plenum (i.e., $\Delta T = T_{corr} - T_{0,i}$). The temperature profiles in Figure 3 to Figure 6 (corresponding to Cases 1 through 4) are orientated such that the reader is aft and looking upstream towards the spray bars. The measured and corrected total temperatures consist of the average TC readings along the sword rake, the average TC readings of the inner and outer duct wall (denoted by the open symbols), and the TAT probe readings, which represent the temperature at the centerline. The $T_{0,i}$ was subtracted from the measured (and corrected) total temperature values to see how the temperatures downstream varied from $T_{0,i}$.

TABLE 2.—THERMOCOUPLE (TC) CORRECTION FACTORS

Sword rake TC	
Mach	Correction
0.2	0.999
.4	.997
.6	.994
.8	.991
.9	.990

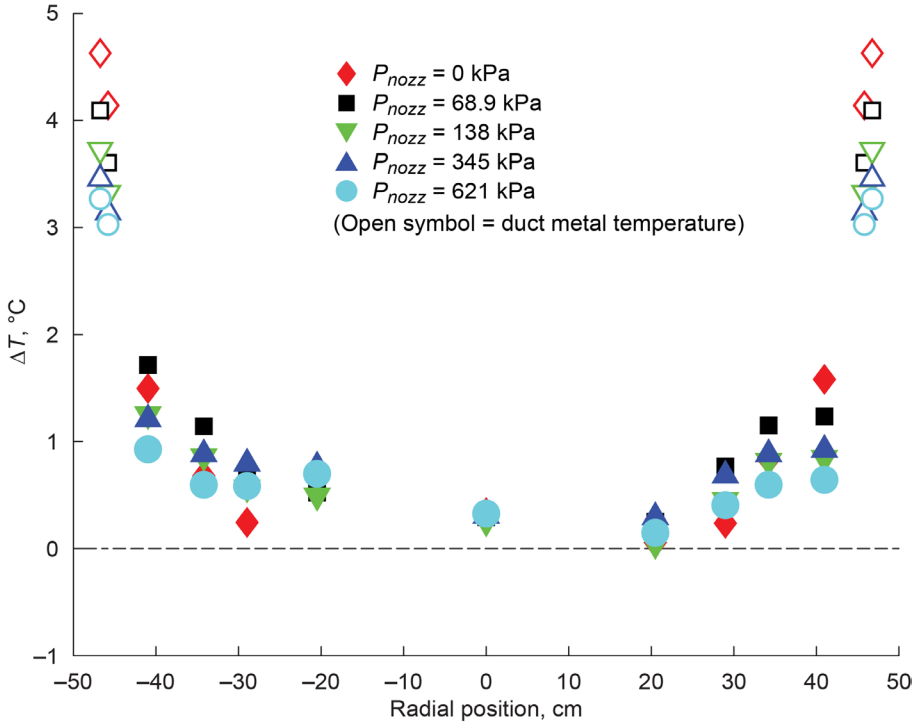

Figure 3.—Case 1 (test runs 3 to 7). Change in temperature (ΔT) versus radial position. Air velocity through calibration duct (V_e) = 85 m/s. Spray-bar atomizing air temperature (T_{nozz}) = total air temperature in the plenum ($T_{0,i}$) = 7.2 °C. Total plenum pressure ($P_{0,i}$) = 87.6 kPa. Spray-bar atomizing air pressure (P_{nozz}).

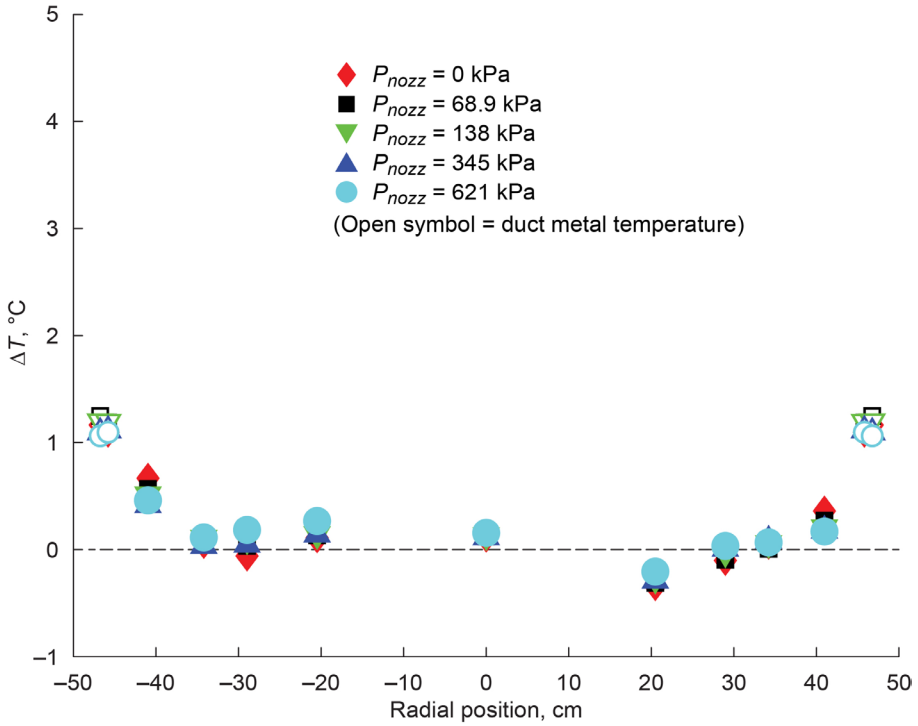

Figure 4.—Case 2 (test runs 18 to 22). Change in temperature (ΔT) versus radial position. Air velocity through calibration duct (V_e) = 135 m/s. Spray-bar atomizing air temperature (T_{nozz}) = total air temperature in the plenum ($T_{0,i}$) = 7.2 °C. Total plenum pressure ($P_{0,i}$) = 87.6 kPa. Spray-bar atomizing air pressure (P_{nozz}).

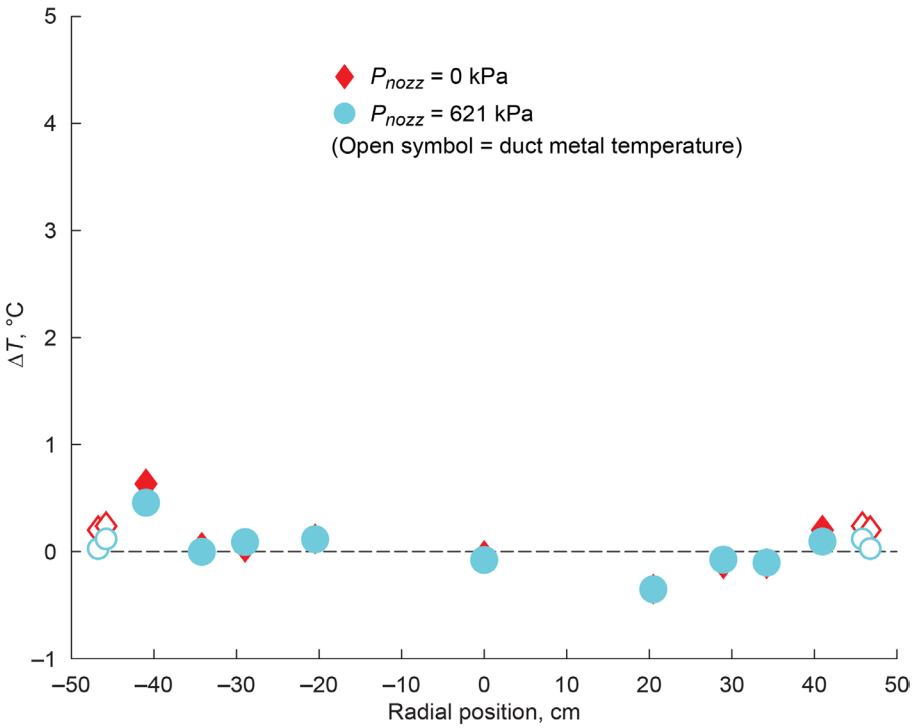

Figure 5.—Case 3 (test runs 25 to 26). Change in temperature (ΔT) versus radial position. Air velocity through calibration duct (V_e) = 185 m/s. Spray-bar atomizing air temperature (T_{nozz}) = total air temperature in the plenum ($T_{0,i}$) = 7.2 °C. Total plenum pressure ($P_{0,i}$) = 87.6 kPa. Spray-bar atomizing air pressure (P_{nozz}).

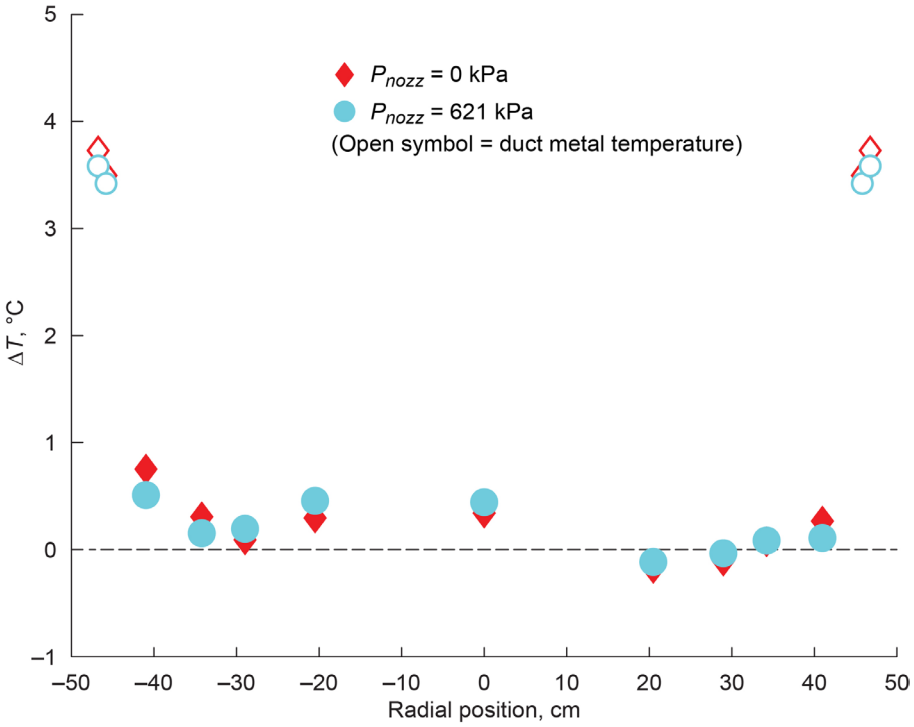

Figure 6.—Case 4 (test runs 36 to 37). Change in temperature (ΔT) versus radial position. Air velocity through calibration duct (V_e) = 85 m/s. Spray-bar atomizing air temperature (T_{nozz}) = total air temperature in the plenum ($T_{0,i}$) = 7.2 °C. Total plenum pressure ($P_{0,i}$) = 44.8 kPa. Spray-bar atomizing air pressure (P_{nozz}).

Figure 3 to Figure 6 show that the temperatures of the duct wall were significantly warmer than the airflow at the lower flow velocities. This is likely caused by convection from the air surrounding the duct, which is generally at ambient temperature and warmer than the flowing air. The ambient temperature surrounding the duct was approximately 22 °C (72 °F) as measured by the RFP in its fully retracted position (approximately 97 cm above the centerline and outside of the flow) at the start of the test. The warmer wall temperatures result in a parabolic temperature profile of the flow. However, as the flow velocity increases, the wall temperature cools down (likely due to the increase in convection heat transfer to the flow), and the temperature profiles flatten out as seen in Figure 4 and Figure 5. Since total temperature is a function of both static temperature and velocity, the fairly uniform total temperature profile across the midsection of the flow indicates that the velocity profile is fairly constant there as well. The temperature profiles seen in Figure 3 to Figure 6 show that the region of flow uniformity extends effectively to a radius of 30 cm (11.8 in.) over which to perform model studies. The figures also show that varying P_{nozz} has very little effect on the downstream temperature profile when T_{nozz} was set to the $T_{0,i}$ of 7.2 °C. However, as will be discussed, changing P_{nozz} will have a considerable effect on the temperature profile when T_{nozz} is much greater than $T_{0,i}$ (T_{nozz} = 82.2 °C).

Figure 6 shows the temperature profile for Case 4 in which the total tunnel pressure was 44.8 kPa (6.5 psi) at an airflow velocity of 85 m/s. When compared to the temperature profile for Case 1 (shown in Figure 3), whose conditions differed only by a higher total tunnel pressure of 87.6 kPa (12.7 psi), there does not seem to be a measurable difference when changing the total tunnel pressure with $T_{nozz} = T_{0,i}$. However, a greater spread in the tunnel wall temperatures can be seen for Case 1 in Figure 3. It is hypothesized that the reason for the greater spread in tunnel wall temperatures shown in Figure 3 is because the tunnel walls, which were cooling slowly due to the lower flow velocity, had not cooled down to their steady-state temperature by the time recording for Case 1 began. Each colder tunnel wall temperature reading in Figure 3 corresponds to a later moment in testing when the tunnel wall temperature was still in the process of cooling down towards its steady-state temperature. For this reason, it is recommended that the tunnel wall temperature be used in addition to the tunnel air temperature as an indicator that the facility has reached thermal equilibrium prior to starting tests.

An interesting phenomenon can be observed from test runs (TRs) 25 and 26 for Case 3 in which the average inner wall temperature of the duct was higher than the average outer wall temperature. This was not expected to occur as the outer wall was exposed to the warm ambient air surrounding the duct, whereas the inner wall was exposed to the cool air inside the duct. A closer analysis of the time histories for Case 3 (shown in Figure 7) reveals that there was a sudden drop in the $T_{0,i}$ during TR 25 as the tunnel flow velocity was increased from 135 to 185 m/s. This is a known operational limit of the PSL when attempting to maintain a steady-state temperature while transitioning to a higher mass flow rate regime. Likewise, lowering the tunnel flow velocity will cause a sudden increase in $T_{0,i}$. To correct for the sudden temperature drop, the PSL facility had to add more heat to the tunnel to bring it back to the target temperature of 7.2 °C. However, the target temperature was overshot and in doing so, there was a period when the flow temperature exceeded the temperature of the duct walls, which resulted in warmer inner wall temperatures for the latter half of TR 25 and through the entirety of TR 26, which began 3 min after TR 25 ended. By averaging the temperature from the last 2 min of testing, the average inner wall temperature was found to be higher than the outer temperature for both TRs 25 and 26.

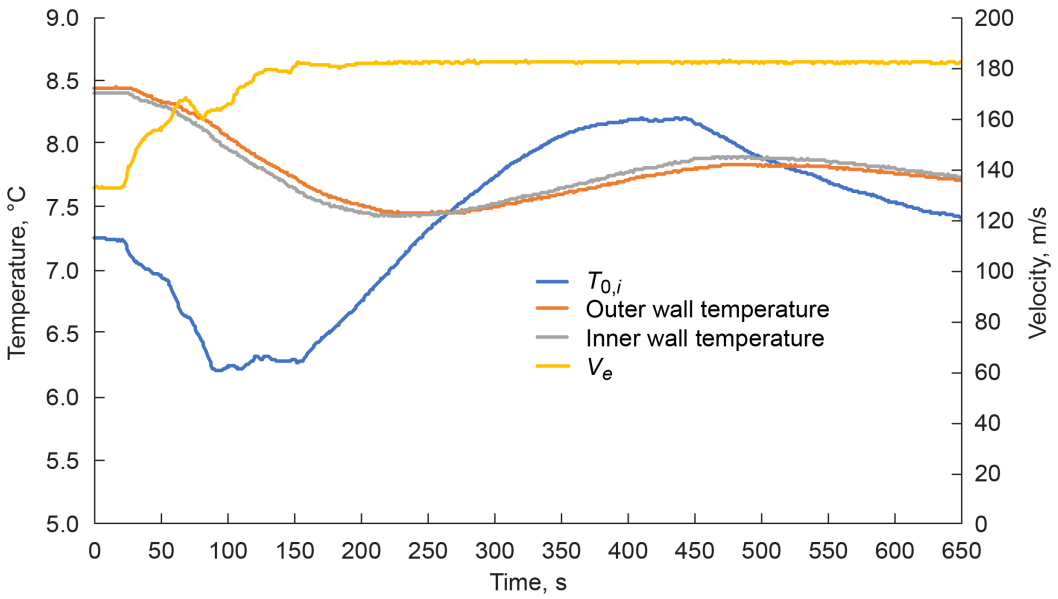

Figure 7.—Case 3 (test run 25) duct temperature and velocity time history. Total air temperature in the plenum ($T_{0,i}$). Air exit velocity through calibration duct (V_e).

An additional investigation was done to see how the spray-bar air temperature influences the downstream temperature profile with P_{nozz} = 0 kPa (gauge) (zero P_{nozz} means no nozzle air flows into the tunnel). For this investigation, two tests at flow velocities of 85 and 185 m/s were conducted while increasing the spray-bar air temperature from the target value of 7.2 to 82.2 °C (some variation exists in the spray-bar air temperatures). Both tests were conducted at a total plenum pressure ($P_{0,i}$) of 44.8 kPa (absolute) and with zero air pressure in the spray bars. A plot of ΔT as a function of radial position for the two tests can be seen in Figure 8 (comparing Cases 4 and 7) and Figure 9 (comparing Cases 5 and 6). The average temperatures used to calculate ΔT were obtained from the last 30 s of the recordings to capture the most steady-state portions of the test. It can be seen from Figure 8 and Figure 9 that increasing the spray-bar target air temperature from 7.2 to 82.2 °C has an uneven effect on the temperature profile. There is almost no effect on the left side of the duct but a slight increase in temperature of up to a half of a degree Celsius on the right side of the duct from the point of view of an observer facing upstream towards the spray bars. This may be caused by the air and water that is transferred to the spray bars through plumbing that enters through the right side of the duct (the water is still circulating through the pipes even though the cloud is turned off). It is hypothesized that the plumbing acts as a heat exchanger that heats the incoming airflow unevenly as the air and water in the plumbing enters through the right side of the duct and cools down as it travels diametrically across the flow to the left side of the duct.

A similar test was done to see the effect of P_{nozz} with T_{nozz} = 82.2 °C. Contrary to the first four cases when T_{nozz} was the same as the $T_{0,i}$ of 7.2 °C, increasing P_{nozz} with T_{nozz} = 82.2 °C steadily increases the temperature at the test section. This is expected since increasing the pressure in the spray bars increases the mass flow rate of air flowing out of the nozzles, which increases the amount of thermal energy added to the tunnel flow due to thermal mixing between the nozzle and the tunnel air. The maximum P_{nozz} that was tested was 621 kPa (gauge) where the temperature at the test section increased by as much as 3 °C at a flow velocity of 85 m/s and 1.5 °C at 185 m/s. This can be seen in Figure 10 and Figure 11, respectively.

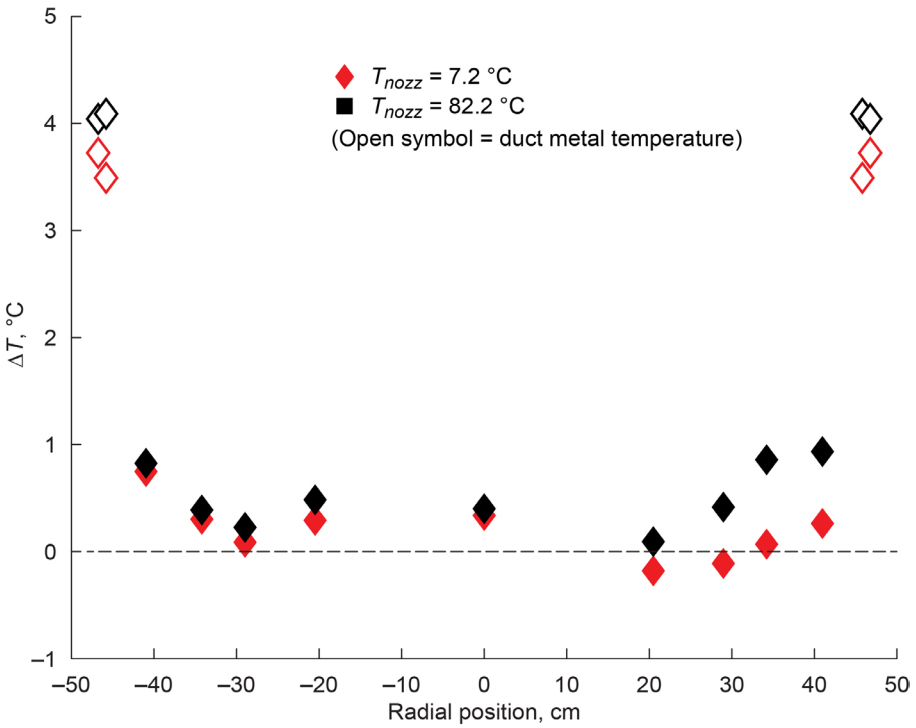

Figure 8.—Case 4 versus Case 7 (test run (TR) 36 versus TR 46). Effect of increasing spray-bar atomizing air temperature (T_{nozz}) to 82.2 °C with spray-bar atomizing air pressure (P_{nozz}) = 0 kPa. Air velocity through calibration duct (V_e) = 85 m/s. Total plenum pressure ($P_{0,i}$) = 44.8 kPa. Change in temperature ΔT.

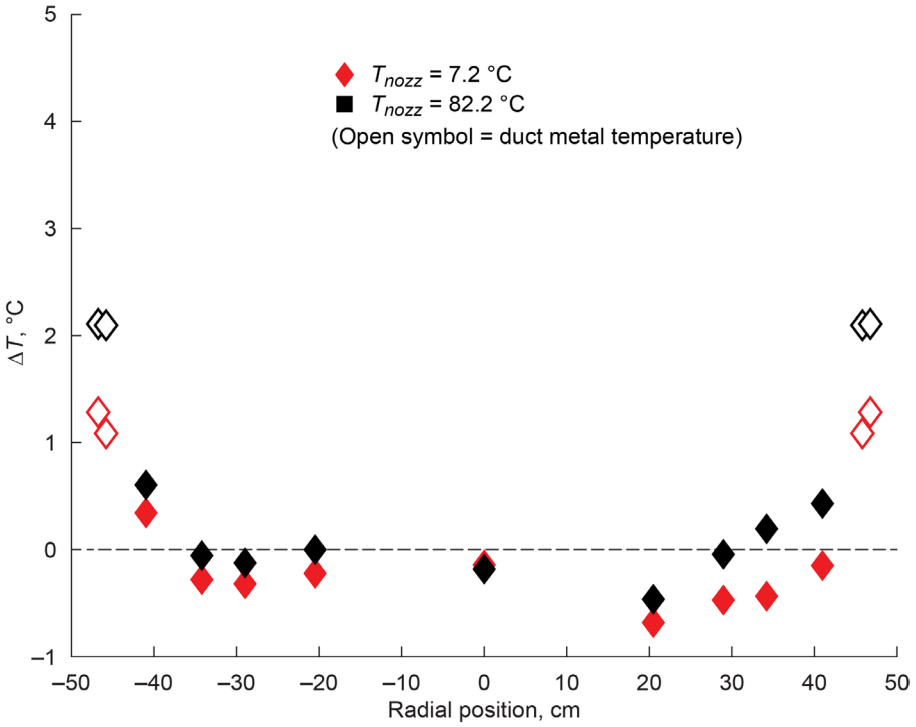

Figure 9.—Case 5 versus Case 6 (test run (TR) 40 versus TR 43). Effect of increasing spray-bar atomizing air temperature (T_{nozz}) to 82.2 °C with spray-bar atomizing air pressure (P_{nozz}) = 0 kPa. Air velocity through calibration duct (V_e) = 185 m/s. Total plenum pressure ($P_{0,i}$) = 44.8 kPa. Change in temperature ΔT.

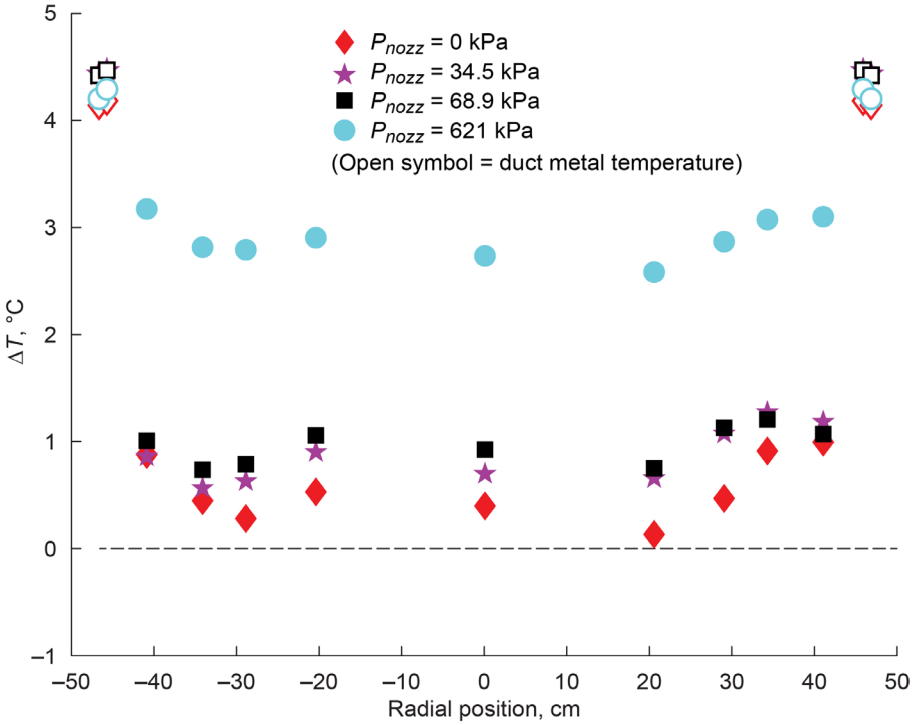

Figure 10.—Case 7 (test run 46). Effect of increasing spray-bar atomizing air temperature (T_{nozz}) to 82.2 °C with spray-bar atomizing air pressure (P_{nozz}) > 0 kPa. Air exit velocity through calibration duct (V_e) = 85 m/s. Total plenum pressure ($P_{0,i}$) = 44.8 kPa. Change in temperature ΔT.

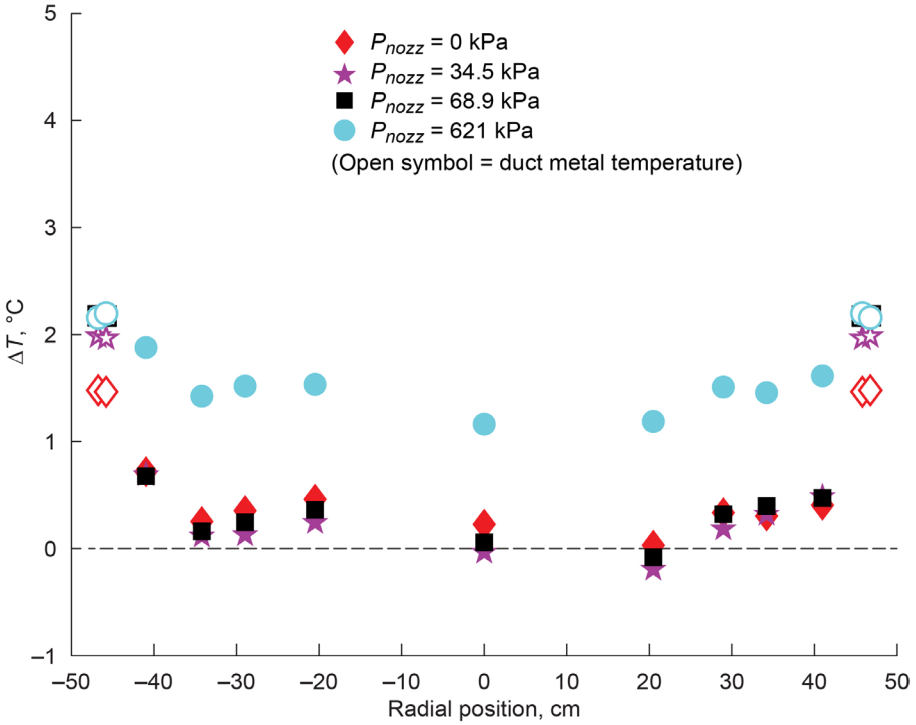

Figure 11.—Case 6 (test runs 43 and 44). Effect of increasing spray-bar atomizing air temperature (T_{nozz}) to 82.2 °C with spray-bar atomizing air pressure (P_{nozz}) > 0 kPa. Air velocity through calibration duct (V_e) = 185 m/s. Total plenum pressure ($P_{0,i}$) = 44.8 kPa. Change in temperature ΔT.

4.3 Rosemount Total Air Temperature Probe Traverse Tests

To compare the temperature readings measured by the TCs of the sword rake and TAT probe, a series of tests were conducted using the traversing mechanism that allowed the TAT probe to move to a corresponding radial and θ location of a particular TC on the sword rake (see Figure 2). It should be noted that the axial location of the TAT probe was downstream of the sword rake containing the TCs (refer to Figure 1). However, since the axial location of the sword rake is currently not known, the distance between the sword rake and the TAT probe was unable to be determined. The first test in the series was done with the TAT probe at a radial distance of 20.4 cm from the centerline corresponding to TC4. This test was repeated three more times by traversing the TAT probe to radial positions of 28.9, 34.1, and 40.9 cm, which correspond to TC3, TC2, and TC1, respectively. The temperature readings from the TAT probe were then compared to the temperature readings from the TCs at the corresponding radial locations, which can be seen in Figure 12 and Figure 13 for airspeeds of 85 and 185 m/s (Cases 1 and 3), respectively. The plots show the temperatures at increasing radial distances when read from left to right and top to bottom.

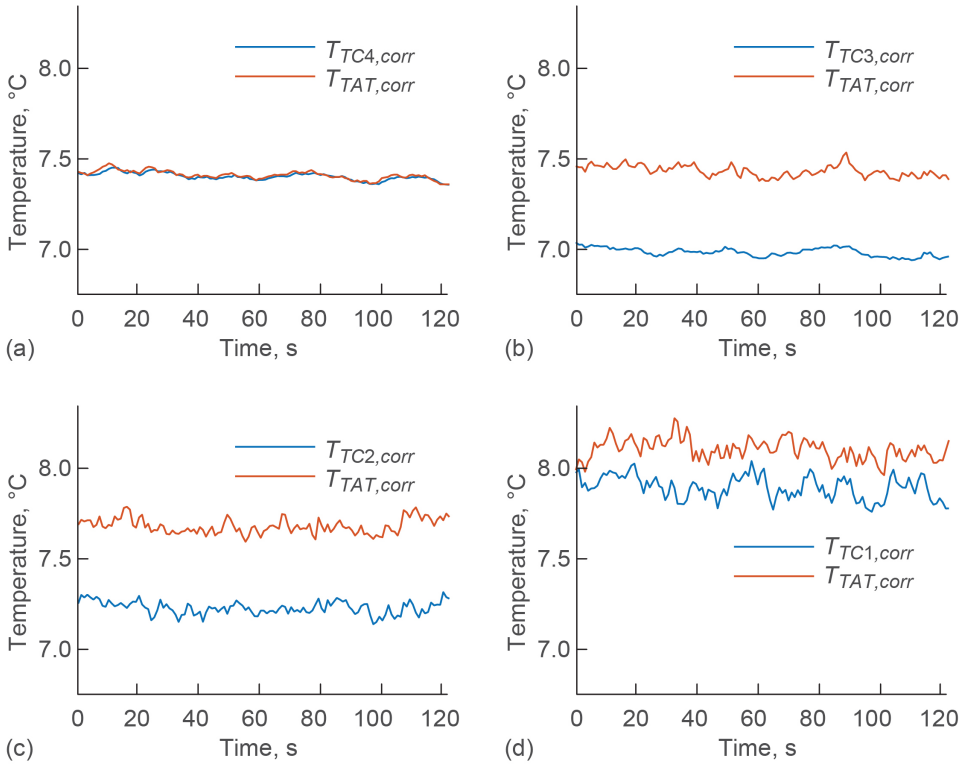

Figure 12.—Case 1 (test runs (TRs) 8 to 11). Total air temperature (TAT) probe versus corresponding thermocouple (TC) temperatures. Air exit velocity through calibration duct (V_e) = 85 m/s. Total plenum pressure ($P_{0,i}$) = 87.6 kPa. Spray-bar atomizing air temperature (T_{nozz}) = 7.2 °C. Spray-bar atomizing air pressure (P_{nozz}) = 0 kPa. Corrected TC temperature ($T_{TC\#,corr}$). Corrected TAT probe temperature ($T_{TAT,corr}$). (a) TR 8. Radial position = 20.4 cm. (b) TR 9. Radial position = 28.9 cm. (c) TR 10. Radial position = 34.1 cm. (d) TR 11. Radial position = 40.9 cm.

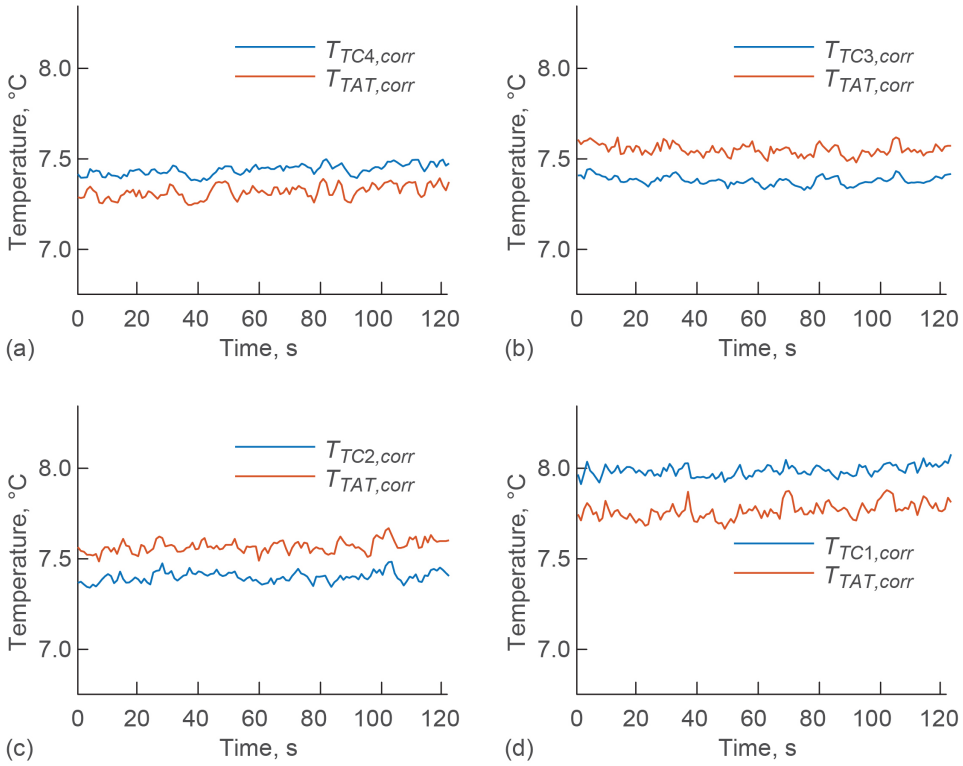

Figure 13.—Case 3 (test runs (TRs) 27 to 30). Total air temperature (TAT) probe versus corresponding thermocouple (TC) temperatures. Air exit velocity through calibration duct (V_e) = 185 m/s. Total plenum pressure ($P_{0,i}$) = 87.6 kPa. Spray-bar atomizing air temperature (T_{nozz}) = 7.2 °C. Spray-bar atomizing air pressure (P_{nozz}) = 0 kPa. Corrected TC temperature ($T_{TC\#,corr}$). Corrected TAT probe temperature ($T_{TAT,corr}$). (a) TR 27. Radial position = 20.4 cm. (b) TR 28. Radial position = 28.9 cm. (c) TR 29. Radial position = 34.1 cm. (d) TR 30. Radial position = 40.9 cm.

One immediate observation that can be made from Figure 12 is that the TC and TAT probe readings were almost identical at the innermost radial position of 20.4 cm at V_e = 85 m/s. As you move radially away from the centerline, the temperature readings seem to fluctuate more indicating that the flow may be less uniform as you move towards the outer radius of the flow. This could also be a possible explanation as to why the TC and TAT probe temperature readings at the innermost location agreed better than the outer locations. For radial positions of 28.9 to 40.9 cm, the difference in temperature readings between the TC and TAT probe varied by no more than half of a degree Celsius, which is within the measurement uncertainty of the temperature probes.

When the airflow velocity was increased to 185 m/s, there did not seem to be a noticeable change in temperature fluctuations with radial position as seen in Figure 13. This suggests that the turbulence intensity across the flow at higher velocities is more uniform across the tested radial distances. The TC and TAT probe readings agreed a lot better for the 185 m/s case than the 85 m/s case with differences no greater than 0.20 °C, still within the measurement uncertainty of the temperature probes.

4.4 Rearward Facing Probe Recovery Correction

For a stationary gas, the total temperature is simply the static temperature of the gas. For a gas that is in motion, the total temperature is the sum of the static and dynamic temperatures of the flow. However, TAT probes, such as the RFP, are unable to recover all the kinetic energy of the moving gas and, therefore,

measure temperatures slightly below the true TAT. Since the amount of unrecovered kinetic energy varies with Mach number, it is convenient to use a recovery correction variable η defined as (Ref. 21):

$$\eta = \frac{T_0 - T_r}{T_0}$$

In this equation, T_0 is the total temperature of the flow and T_r is the recovery temperature where both are in absolute temperature units. In this case, the T_0 is assumed to be equal to $T_{0,i}$ and the T_r is the uncorrected total temperature measured by the RFP sensor ($T_{RFP,m}$).

Figure 14 and Figure 15 show plots of the $T_{RFP,m}$ and the radial position of the RFP (R_{RFP}) for Mach numbers of 0.25 and 0.57, respectively. Both cases were at the same target $T_{0,i}$ of 7.2 °C and $P_{0,i}$ of 87.6 kPa. $T_{0,i}$ is plotted as a dotted line for reference.

The radial position of the RFP is initially outside of the test section at a distance of approximately 71 cm (28 in.) from the centerline as seen by the orange line in Figure 14 and Figure 15. During this time, the RFP is measuring the ambient air temperature surrounding the duct, which is generally much warmer than the airflow in the duct. Shortly after recording begins, the RFP is lowered towards the centerline of the test section via the traversing mechanism. The RFP enters the flow at a radial position of 45.7 cm (18 in.) and takes approximately 2 min to stabilize at a new temperature for both the 85 and 185 m/s cases. Once stabilized, there is a significant difference between the $T_{0,i}$ and the $T_{RFP,m}$. This is attributed to

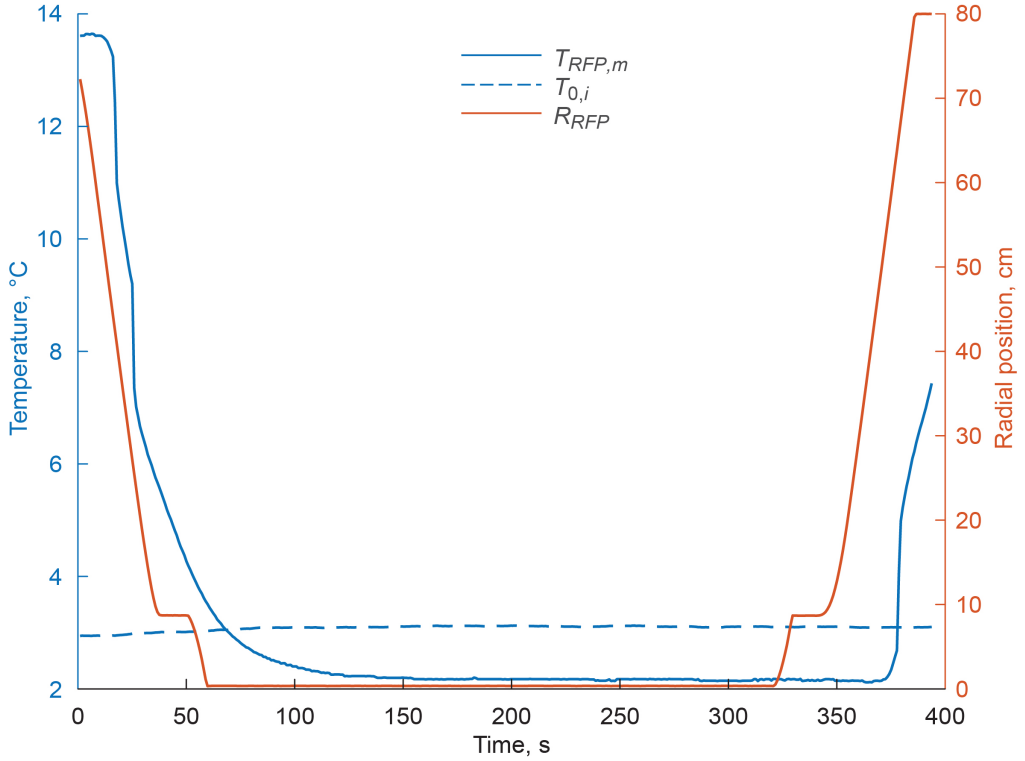

Figure 14.—Case 1 (test run 13). Rearward facing probe (RFP) temperature measurements at Mach 0.25. Air exit velocity through calibration duct (V_e) = 85 m/s. Total plenum pressure ($P_{0,i}$) = 87.6 kPa. Spray-bar atomizing air temperature (T_{nozz}) = 7.2 °C. Spray-bar atomizing air pressure (P_{nozz}) = 0 kPa. Recovery (uncorrected) temperature is the total temperature measured by the RFP sensor ($T_{RFP,m}$). Total plenum temperature ($T_{0,i}$). Radial position of the RFP (R_{RFP}).

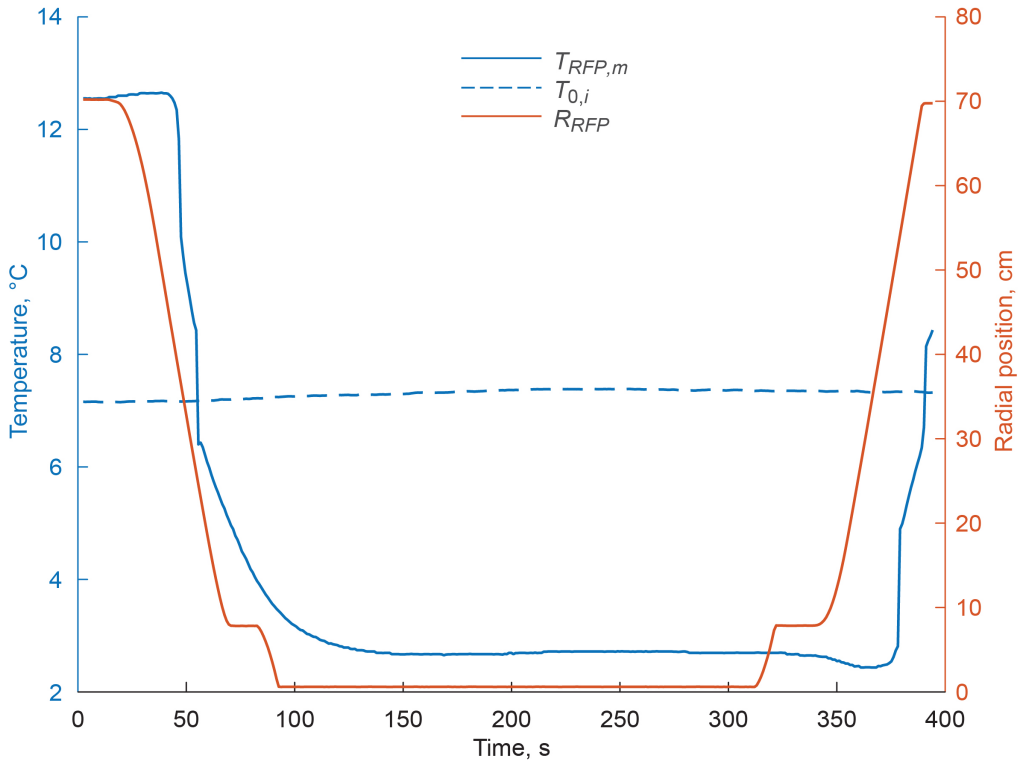

Figure 15.—Case 3 (test run 32). Rearward facing probe (RFP) temperature measurements at Mach 0.57. Air exit velocity through calibration duct (V_e) = 185 m/s. Total plenum pressure ($P_{0,i}$) = 87.6 kPa. Spray-bar atomizing air temperature (T_{nozz}) = 7.2 °C. Spray-bar atomizing air pressure (P_{nozz}) = 0 kPa. Recovery (uncorrected) temperature is the total temperature measured by the RFP sensor ($T_{RFP,m}$). Total plenum temperature ($T_{0,i}$). Radial position of the RFP (R_{RFP}).

the high recovery correction factor corresponding to the high Mach number as discussed earlier. For the Mach 0.25 (85 m/s) case shown in Figure 14, the difference in temperature is not as substantial due to the lower recovery correction as expected.

Figure 16 shows a plot of the recovery correction as a function of Mach number. The first data point was constrained at the origin as it is assumed that the recovery correction for an unmoving mass of air is zero. The remaining three data points were taken from the recovery correction values calculated from the RFP data at Mach numbers of 0.25, 0.41, and 0.57, respectively. At first glance, the curve-fit through the data points (represented by the gray line in Figure 16) appears to be nonlinear as one would expect for the relationship between recovery correction and Mach number. However, it should be noted that the curve would resemble more of a linear relationship if the point at the origin were to be removed. A similar plot was made by Agui, Struk, and Bartkus for RFP measurements at different relative humidities (Ref. 21). The recovery correction curve calculated for that test is represented by the blue line in Figure 16. The recovery corrections calculated by Agui at different relative humidities are very similar to the recovery corrections presented here during which the relative humidity was zero. This would support Agui's conclusion that relative humidity does not have a significant effect on the recovery correction.

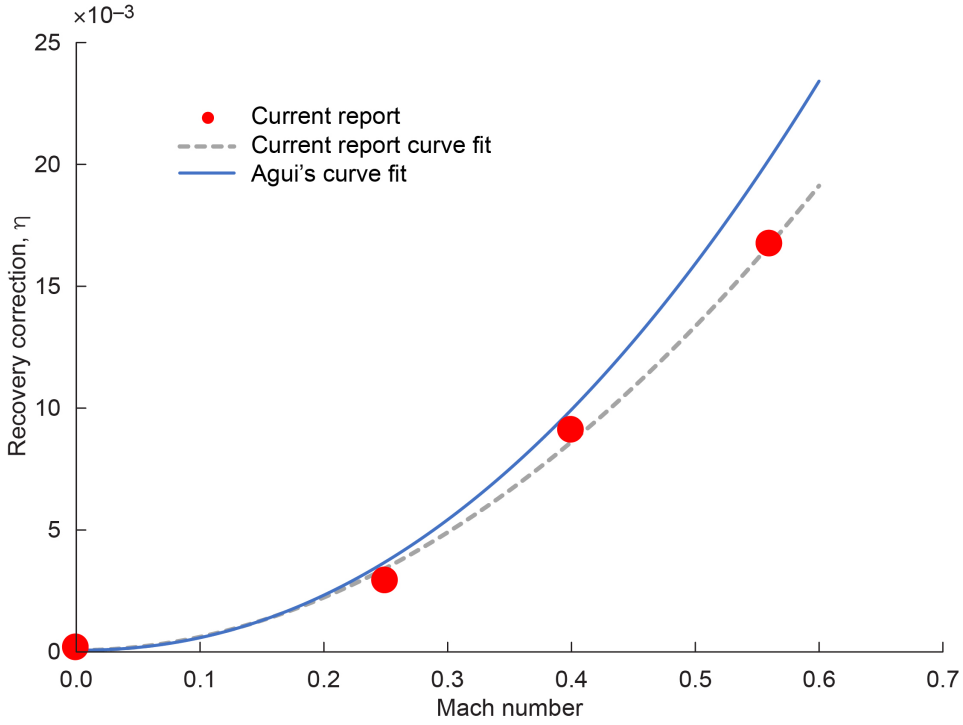

Figure 16.—Cases 1 to 3 (test runs 13, 24, and 32). Rearward facing probe (RFP) recovery correction. Total plenum pressure ($P_{0,i}$) = 87.6 kPa. Spray-bar atomizing air temperature (T_{nozz}) = 7.2 °C. Spray-bar atomizing air pressure (P_{nozz}) = 0 kPa. Current report curve fit $\eta = 0.05246 \cdot M^{1.974}$. Agui's curve fit (Ref. 21) $\eta = 0.06916 \cdot M^{2.1195}$.

4.5 Rosemount Total Air Temperature Probe Heat On and Off Comparison

During icing conditions, the TAT probe is susceptible to ice buildup at the inlet and around the sensor that can lead to false temperature readings. To counter this, the TAT probe comes equipped with a deicing heat element to melt any accreting ice formations on the probe. However, in heating the probe, the deicing heat element itself can cause the TAT probe to read temperatures slightly higher than the TAT. To see the effects of these deicing-heat-induced errors, the TAT probe was inserted into the flow to measure the temperature at three airflow velocities; first with the heating element turned off and then with the heating element turned on.

Figure 17 shows a plot of ΔT at three different Mach numbers where ΔT is the difference between the average corrected temperature from the TAT probe and the $T_{0,i}$ with either the heating element in the TAT probe turned off (shown in blue) or turned on (shown in red). The typical 2-min timeframe from the end of the recording used to calculate the average temperature values could not be used for the heat-on tests as the data recordings started before the heat was applied and concluded after the heat was turned off. As a result, care was taken to use data only during the heat-on phase, which had to be determined for TRs 12, 23, 31, and 38 individually. The majority of the tests were conducted at a $P_{0,i}$ = 87.6 kPa (absolute) at a Mach number of either 0.25, 0.41, or 0.57 corresponding to TRs 3, 18, and 25 for the heat-off case or 12, 23, and 31 for the heat-on case, respectively. When comparing ΔT between the heat-off and heat-on cases at a $P_{0,i}$ = 87.6 kPa (absolute), it can be seen that the TAT probe reads temperatures approximately 0.7 °C warmer with the deicing heat element turned on. An extra test was done for both the heat-off and heat-on cases (corresponding to TRs 36 and 38, respectively) at Mach 0.25 at a $P_{0,i}$ = 44.8 kPa (absolute) (represented by the open star symbols in Figure 17) to see the effect of reducing the total pressure. From

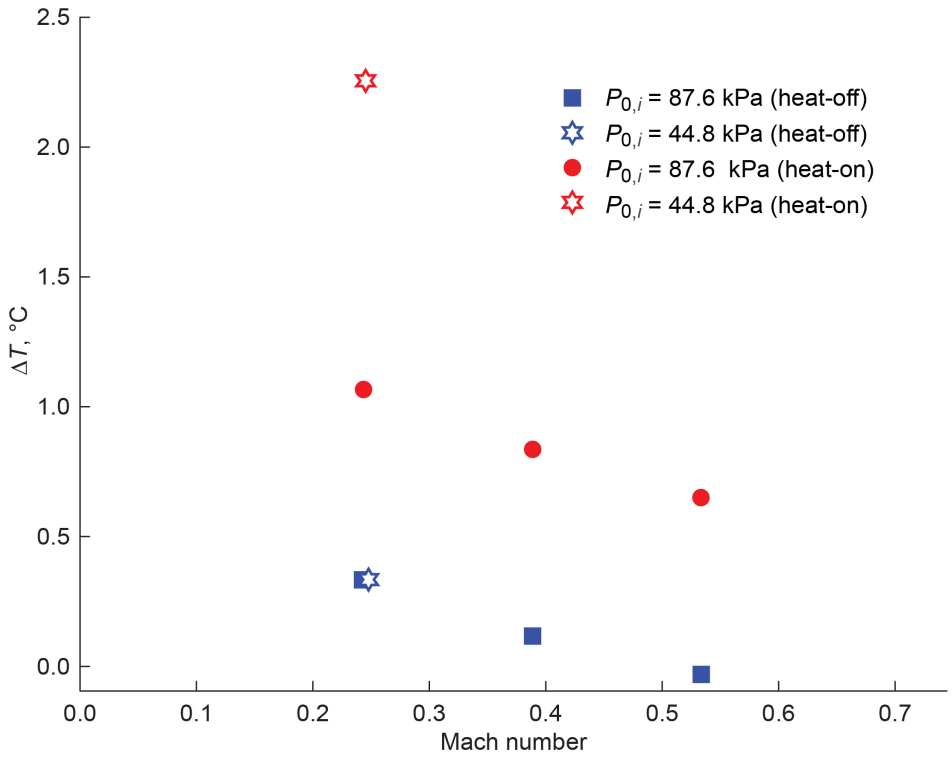

Figure 17.—Change in temperature ΔT = temperature of Rosemount total air temperature (TAT) probe heat on or off ($T_{TAT,\text{heat-on or heat-off}}$) – total plenum temperature ($T_{0,i}$) at various Mach numbers (heat-off: test runs (TRs) 3, 18, 25, and 36 and heat-on: TRs 12, 23, 31, and 38). Total plenum pressure ($P_{0,i}$).

this, we can see that lowering the $P_{0,i}$ from 87.6 to 44.8 kPa (absolute) increases the deicing-heat-induced error as the TAT probe measures temperatures about 1.9 °C higher with the heating element turned on than with the heating element turned off. This is expected to occur as there are less air molecules for the excess energy produced by the heating element to be transferred to. The ΔT values for the heat-off case are consistent with the centerline ΔT values measured by the TAT probe during the sword rake tests discussed earlier in the report.

5.0 Conclusions

This report documents some of the key findings from the aerothermal calibration test that was conducted at the NASA Propulsion Systems Laboratory (PSL) in 2018. This test utilized a newly developed traversing mechanism, which allowed centerline measurements and radial surveys of the flow to be made. The aerothermal calibration test data was used to characterize the temperature profiles at the test section during various cloud-off conditions. The data indicates that there is negligible change in the test section temperature caused by altering the spray-bar atomizing pressure when the spray-bar air temperature is the same as the plenum temperature (in this case, 7.2 °C). When the spray-bar air temperature and pressure were raised to 82.2 °C and 621 kPa, respectively, the temperature at the test section increased by as much as 3 °C at an airflow velocity of 85 m/s due to thermal mixing of the warmer air from the nozzles to the tunnel flow.

Increasing the spray-bar air temperature to 82.2 °C without turning on the nozzle airflow had an uneven effect on the temperature profile at the test section. There was negligible temperature change on the left side of the duct while the air temperature on the right side of the duct increased by 0.5 °C from the point of view of an observer facing upstream towards the spray bars. It is hypothesized that the plumbing that carries the water and air to the spray bars, which is still circulating during cloud-off conditions, acts as a heat exchanger that heats the flow unevenly as it enters through the right side of the duct.

The data also reveals that the metal walls of the duct can be much warmer than the flow due to the warm ambient air surrounding the test section. This resulted in parabolic temperature profiles with the air having higher temperatures near the duct wall than at the centerline. It is recommended that the duct wall temperatures be monitored to ensure that they have reached a steady-state prior to testing. In addition, it is recommended that model studies be performed within a 30-cm radius of the centerline over which the temperature profile is the most uniform.

Comparisons were made between the sword rake thermocouples (TCs) and total air temperature (TAT) probe on the traversing system, which were in the same radial and azimuthal positions but different axial locations near the test section. This data showed the TC and TAT probe readings agreed to within 0.5 °C, which is within measurement uncertainty, for all positions with the best agreement occurring at the innermost radial position. Further away from the centerline, the temperature readings fluctuated more, particularly at the lower airspeed of 85 m/s, indicating that the flow may not be as uniform at this lower mass flow condition at PSL.

Selected cases of rearward facing probe data were presented in this report as well as a calculation of the probe's thermal recovery correction as a function of Mach number. The results were similar to those reported earlier, which show a slow thermal response of close to 2 min when the probe was inserted from a quiescent flow into a flow with cooler total temperature. Furthermore, the probe requires a significant recovery correction due to the rearward facing inlet of the probe.

Finally, the Rosemount TAT probe deice heat correction was characterized during testing. At a plenum total pressure of 87.6 kPa, the deice heat correction at a Mach number of 0.25 was 0.7 °C. That correction increased to 1.9 °C when the total pressure was reduced to 44.8 kPa at the same Mach number.

Appendix—Sword Rake Calibration

The sword rake, which spans the 0.91-m diameter of the constant area duct, uses type-K thermocouples (TCs) and pressure probes that are alternately spaced with a pressure port at the axial centerline (Figure 18). The TCs and pressure ports face upstream into the oncoming flow. In order to measure the most accurate total or stagnation temperature, it is necessary to bring the flow to rest at the TC in an isentropic manner. To this end, researchers installed aspirated tips onto each TC to bring the flow to rest in an isentropic manner. The aspirated tips were designed per NASA empirical standards (reference drawing CC–152916 dated Aug. 16, 1977). Researchers calibrated each aspirated-tip TC in the free-jet facility Probe Calibration Laboratory, also called the CE–12, at NASA Glenn Research Center. The CE–12 facility provides known total temperature and mass flow in an 8.9-cm (3.5-in.) free jet such that researchers can characterize various probes. The CE–12 facility is capable of producing flows of Mach 0.05 to 0.90 at stagnation temperatures between ambient air temperature and 93 °C (200 °F).

The characterization tests had the aspirated-tip TCs centered on the CE–12 nozzle outlet as seen in Figure 19. Researchers varied the Mach number from 0.1 to 0.9 while holding the total temperature constant. By comparing the measured total temperature ($T_{TC\#}$) to the known total temperature (T_0) produced by the CE–12 facility at various Mach number flows, researchers were able to develop a characterization curve for the individual TCs on the sword rake as a function of Mach number. Table 3 shows the averaged ratio of $T_{TC\#}$ to T_0 for various probes on the sword rake (T_{TC1} to T_{TC8}) at various Mach numbers. The data indicates that the probe position on the sword rake was nearly negligible as compared to the Mach number.

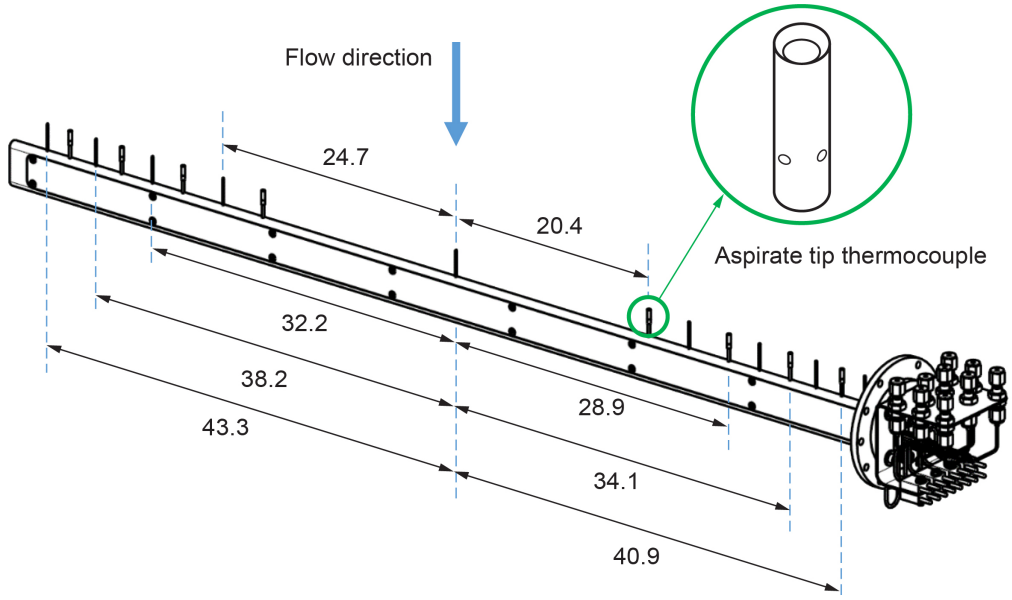

Figure 18.—Sword rake. Dimensions are in centimeters.

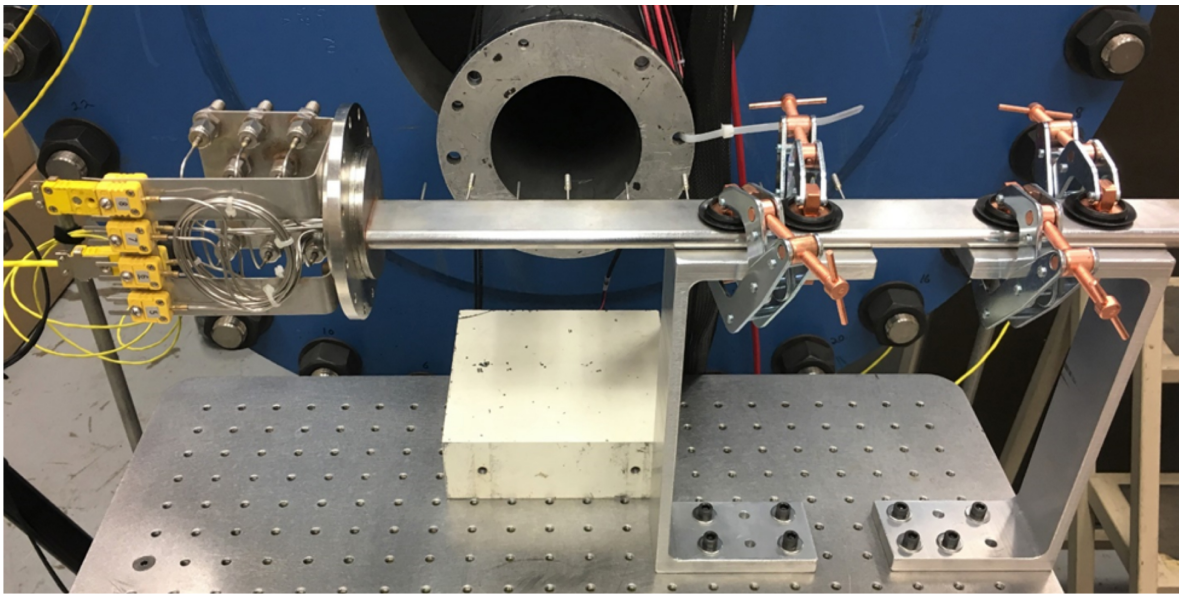

Figure 19.—Typical thermocouple characterization test setup, probe 7 shown. Probe 8 is nearest to bulkhead at left of figure.

TABLE 3.—AVERAGED DATA FROM ASPIRATED TIP THERMOCOUPLE (TC) CHARACTERIZATION TEST
[Temperature of the TC ($T_{TC\#}$). Total plenum temperature (T_0).]

Mach	T_{TC1}/T_0	T_{TC2}/T_0	T_{TC3}/T_0	T_{TC4}/T_0	T_{TC5}/T_0	T_{TC6}/T_0	T_{TC7}/T_0	T_{TC8}/T_0
0.10	1.000	1.000	1.000	1.000	0.999	1.000	1.000	1.000
.20	.999	.999	.999	.999	.999	.999	.999	.999
.30	.998	.998	.998	.998	.998	.998	.998	.998
.40	.997	.997	.997	.996	.997	.997	.997	.997
.50	.996	.995	.996	.995	.995	.996	.995	.996
.60	.995	.994	.994	.993	.993	.994	.993	.994
.70	.993	.993	.993	.992	.992	.993	.992	.993
.79	.992	.991	.992	.990	.990	.991	.990	.991
.90	.990	.989	.989	.988	.987	.988	.986	.990

References

1. Mason, Jeanne G.; Strapp, J. Walter; and Chow, Philip: The Ice Particle Threat to Engines in Flight. AIAA 2006–206, 2006.
2. Griffin, Thomas A.; Dicki, Dennis J.; and Lizanich, Paul J.: PSL Icing Facility Upgrade Overview. AIAA 2014–2896, 2014.
3. Oliver, Michael J.: Validation Ice Crystal Icing Engine Test in the Propulsion Systems Laboratory at NASA Glenn Research Center. AIAA 2014–2898, 2014.
4. Oliver, M.: Ice Crystal Icing Engine Testing in the NASA Glenn Research Center's Propulsion Systems Laboratory: Altitude Investigation. SAE Int. J. Aerosp., vol. 8, no. 1, 2015, pp. 33–37.
5. Flegel, Ashlie B.; and Oliver, Michael J.: Preliminary Results From a Heavily Instrumented Engine Ice Crystal Icing Test in a Ground Based Altitude Test Facility. AIAA 2016–3894, 2016.
6. Struk, P., et al.: Fundamental Ice Crystal Accretion Physics Studies. NASA/TM—2012-217429 (SAE–2011–38–0018), 2011. https://ntrs.nasa.gov
7. Currie, Tom C., et al.: Fundamental Study of Mixed-Phase Icing With Application to Ice Crystal Accretion in Aircraft Jet Engines. AIAA 2012–3035, 2012.
8. Struk, Peter M., et al.: Ice Crystal Icing Physics Study Using a NACA 0012 Airfoil at the National Research Council of Canada's Research Altitude Test Facility. AIAA 2018–4224, 2018.
9. Flegel, A.B.: Ice Crystal Icing Research at NASA Glenn Research Center. AIAA 2017–4085, 2017.
10. Wright, William B.; Jorgenson, Philip C.E.; and Veres, Joseph P.: Mixed Phase Modeling in GlennICE With Application to Engine Icing. AIAA 2010–7674, 2010.
11. Tsao, Jen-Ching; Struk, Peter M.; and Oliver, Michael J.: Possible Mechanisms for Turbofan Engine Ice Crystal Icing at High Altitude. AIAA 2014–3044, 2014.
12. Currie, Thomas C.; Fuleki, Dan; and Mahallati, Ali: Experimental Studies of Mixed-Phase Sticking Efficiency for Ice Crystal Accretion in Jet Engines. AIAA 2014–3049, 2014.
13. Villedieu, Philippe; Trontin, Pierre; and Chauvin, Remi: Glaciated and Mixed Phase Ice Accretion Modeling Using ONERA 2D Icing Suite. AIAA 2014–2199, 2014.
14. Wright, William B., et al.: Recent Advances in the LEWICE Icing Model. SAE 2015–01–2094, 2015.
15. Bartkus, Tadas P.; Struk, Peter; and Tsao, Jen-Ching C.: Development of a Coupled Air and Particle Thermal Model for Engine Icing Test Facilities. SAE Int. J. Aerosp., vol. 8, no. 1, 2015, pp. 15–32.
16. Bartkus, Tadas P.; Struk, Peter M.; and Tsao, Jen-Ching: Evaluation of a Thermodynamic Ice Crystal Icing Model Using Experimental Ice Accretion Data. AIAA 2018–4129, 2018.
17. Bartkus, T.P.; Tsao, J.-C.; and Struk, P.M.: Analysis of Experimental Ice Accretion Data and Assessment of a Thermodynamic Model During Ice Crystal Icing. SAE 2019–01–2016, 2019.
18. Struk, Peter M., et al.: Ice-Crystal Icing Accretion Studies at the NASA Propulsion Systems Laboratory. SAE 2019–01–1921, 2019.
19. Struk, Peter M., et al.: An Initial Study of the Fundamentals of Ice Crystal Icing Physics in the NASA Propulsion Systems Laboratory. AIAA 2017–4242, 2017.
20. Stickney, Truman M.; Shedlov, Marvin W.; and Thompson, Donald I.: Goodrich Total Temperature Sensors. Rosemount Aerospace Inc. Technical Report 5755, Revision C, 1994.
21. Agui, Juan H.; Struk, Peter; and Bartkus, Tadas: Total Temperature Measurements in Icing Cloud Flows Using a Rearward Facing Probe. SAE 2019–01–1923, 2019.
22. Agui, Juan H.; Struk, Peter M.; and Bartkus, Tadas P.: Total Temperature Measurements Using a Rearward Facing Probe in Supercooled Liquid Droplet and Ice Crystal Clouds. AIAA 2018–3970, 2018.